Cobalt Nanocrystals Encapsulated in Heteroatom-Rich Porous Carbons Derived from Conjugated Microporous Polymers for Efficient Electrocatalytic Hydrogen Evolution

Haige Wang[1], Bo Hou[3], Yang Yang[4], Qianwang Chen[4], Meifang Zhu[1,], Arne Thomas[2]*, Yaozu Liao[1,2]**

[1]State Key Laboratory for Modification of Chemical Fibers and Polymer Materials & College of Materials Science and Engineering, Donghua University, Shanghai 201620, China

[2]Department of Chemistry and Functional Materials, Technische Universität Berlin, Berlin 10623, Germany

[3]Department of Engineering Science, University of Oxford, OX1 3PJ, Oxford, U.K

[4]Hefei National Laboratory for Physical Sciences at Microscale and Department of Materials Science & Engineering, University of Science and Technology of China, Hefei, China

Corresponding Author: yzliao@dhu.edu.cn;arne.thomas@tu-berlin.de and zmf@dhu.edu.cn

Enabling an efficient hydrogen evolution reaction (HER) using earth-abundant metal catalysts is one of the most significant challenges in electrocatalysis. Cobalt nanocrystals encapsulated in nitrogen and oxygen dual-doped porous carbon is such an efficient and stable electrocatalyst for HER. Microporous, heteroatom-rich polymer networks, which are applied as carbon precursor and metal support, can be deposited directly on carbon fiber cloth, removing the necessity of using any binder for the preparation of the electrocatalyst. This electrocatalyst, with remarkably low cobalt loading (1.35 wt%), achieves a Tafel slope of 46 mV dec^{-1} and an overpotential of only 69 mV at a current density of 10 mA cm^{-2} in 0.5 M sulfuric acid solution. Surface structural and computational studies reveal that the superior behavior is owing to the decreased ΔG_{H*} for HER.

Electrocatalytic water splitting represents one of the most promising pathways to produce hydrogen as a sustainable fuel.[1] The development of active electrocatalysts is crucial to promote the hydrogen and oxygen evolution rate and reduce the overpotentials of these reactions. Platinum (Pt) supported on activated carbons is currently the benchmark catalyst for the hydrogen evolution reaction (HER), but has its drawbacks in scarcity and high-cost of the active compound.[2] In recent years, many research efforts have been devoted to find non-noble metal compounds as possible alternatives for HER catalysts. Earth-abundant transition metal (e.g. Co, Ni or Mo) compounds have been shown to be promising catalytic materials for HER in alkaline electrolytes.[3,4] Nevertheless, many of these compounds are not stable in acidic media, needed for an efficient HER.[5] Recently, transition metal-based nanoparticles encapsulated in carbons have attracted considerable attentions to promote the HER activity and stability.[6-10] However, these materials are often prepared by complex multi-step syntheses, again raising issues about cost and scalability. A facile synthesis of low-cost and acid-stable HER catalysts would be therefore highly desirable.[11] Experimental and theoretical results have shown that single or dual heteroatom doping of carbonaceous materials, with nitrogen, sulfur, phosphine or boron can significantly improve the HER performance.[12-15] Herein, we apply a conjugated microporous polymer (CMP) as precursor for a unprecedented nitrogen (N) and oxygen (O) dual-doped carbon with encapsulated metal (Co) nanoparticles, which indeed show superior performance as HER catalyst.

CMPs provide large specific surface areas and high chemical stability. These features make them promising materials for gas uptake, catalysis, and energy storage applications.[16] CMPs furthermore are interesting materials for the rational design of heteroatom-doped porous carbon materials.[17] We have recently shown, that using the Buchwald-Hartwig coupling,[18] N and O-rich (>20 wt%) CMPs with 2,6-

diaminoanthraquinonylamine (DAQ) and triphenylamine (TA) moities (i.e. PAQTA) can be easily synthesized and perform excellent electrochemical energy storage performance. Owing to its cross-linked network structure and intrinsic porosity as well as the high amount of heteroatoms, PAQTA seems to be a promising support for metal nanoparticles and precursor for heteroatom-doped porous carbon materials. We herein demonstrate a scalable and straightforward pyrolysis route to metallic cobalt nanoparticles (CoNPs) encapsulated in N,O-dual doped carbons (CoNOCs) as HER catalysts using PAQTA networks as precursors. The fabrication of binder-free membrane-like HER electrodes is possible through the deposition of the catalysts on woven carbon fiber cloth (CFC). The high flexibility of the resulting electrodes allows scaling-up the catalytic setup.

Results

Preparation and characterization of CoNOCs. The bulk CoNOC-x catalysts were prepared by impregnating PAQTA with $Co(acac)_2$ in a first step, followed by pyrolysis under N_2 atmosphere at four temperatures (i.e. 700, 800, 900, and 1000 ^oC, x indicates the pyrolysis temperature) followed by removal of weakly bound metal species by etching with aqueous sulfonic acid (Fig. 1a,b). where. Metal-free carbon catalysts named NOC-x were prepared in absence of $Co(acac)_2$ for comparison. The Fourier-Transform Infrared (FT-IR) spectrum of $Co(acac)_2$ impregnated PAQTA show a very similar pattern to the pristine precursor (Fig. 1c).[18] Raman spectra were measured to investigate the graphitization of CoNOCs. All spectra show two peaks at 1585 and 1345 cm^{-1} associated with the D and G bands (Fig. 2d), respectively. With increasing temperature from 700 to 1000 ^oC, the ratio of the intensity of the D to the G band (I_D/I_G) decreased from 1.14 to 0.89, indicating increasing graphitization. The I_D/I_G value is often used as a measure of defect density in graphite.[19,20] In the case of CoNOCs, the I_D/I_G maintained at high values, suggesting the presence of significant structural defects presumably due to the presence of N and O dopants. It was suggested that these defects could promote the HER electroactivity because more catalytic sites are exposed.[21] The PXRD pattern of CoNOC-900 before acid etching showed three sharp peaks at 44.2, 51.5, and 75.6^o (Fig. 1e), which are representing the characteristic (111), (200), and (220) reflections of cubic Co,[22] respectively. Additionally, the product showed two small peaks at 41.5 and 47.3^o probably due to the formation of CoO. It can be assumed that during the acid treatment cobalt compounds which are easier accessible, e.g. not fully encapsulated in the carbon matrix will be primarily etched out. Indeed the diffraction peaks attributed to metal species are not detectable for CoNOC-900 and CoNOC-1000, but still visible for CoNOC-700 and CoNOC-800, however with much lower intensity. Inductively coupled plasma mass spectrometry (ICP/MS) and elemental analysis (EA) measurements indicate that 2.45, 1.13, 0.46, and 0.17 wt% of Co, along with 3.45, 2.08, 1.35, and 1.17 wt% of N remained in CoNOC-700, CoNOC-800, CoNOC-900, and CoNOC-1000 (Table S1), respectively.

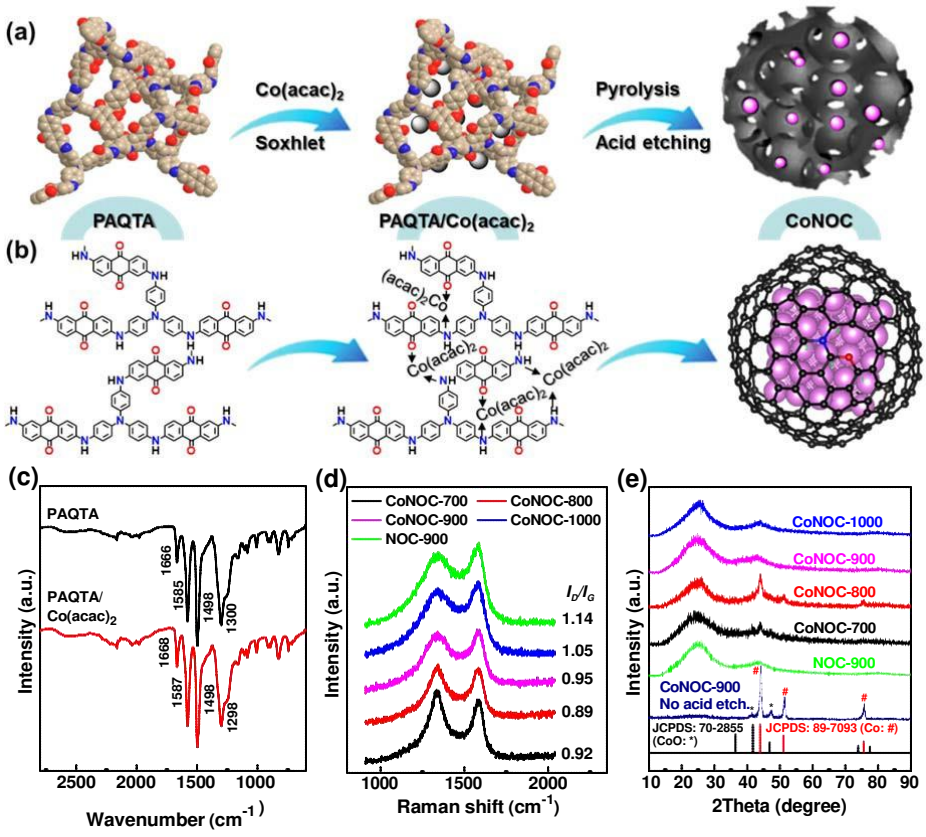

Fig. 1 Preparation and characterization of CoNOCs. (a,b) Synthetic schemes, (c) FT-IR, (d) Raman, and (e) PXRD spectra of the CoNOCs.

As shown by the scanning electron microscopy (SEM) images (Figs. 2a, S1), the agglomerates of CoNOCs consist of particles with diameters of 50-100 nm. With increasing pyrolysis temperature, it appears that the nanoparticles tend to form sheet-like structures owing to the increased graphitization. Transmission electron microscopy (TEM) measurements for CoNOC-900 (Fig. 2b), furthermore show the formation of small Co nanoparticles (CoNPs) with an average diameter of *ca.*10 nm within the porous carbon structure. Diffused ring patterns were observed from the selected-area electron diffraction (SAED) analysis of one CoNP which determed the polycrystalline nature of the CoNPs (Fig. 2c).[23] Sensitive high angle annular dark field (HAADF) scanning transmission electron microscopy (STEM) imaging combined with energy-dispersive X-ray spectroscopy (EDX) elemental mapping further proves the presence and uniform distribution of N and Co within the carbon matrix (Fig. 2d-f and Figs. S2-4). HAADF STEM and atomic-scale high-resolution TEM (HRTEM) characterizations furthermore show that the CoNPs are tightly encapsulated by graphitic carbon (Fig. 2e,h,i). As can be seen in the Fig. 2g-i, two lattice fringes are measured to be ~0.20 and ~0.24 nm, which are consistent with the (111) and (002) lattice parameters for the cubic bulk Co nanocrystal cores and graphitic shells (Fig. S5),[24] respectively. Note that the graphitic shells exhibit 5-15 layers. Before acid washing, a larger population of CoNPs with an average diameter of *ca.* 10 nm can be seen from HRTEM analysis (Fig. S6), which implies that the remaining CoNPs after acid washing are well encapsulated in CoNOCs.

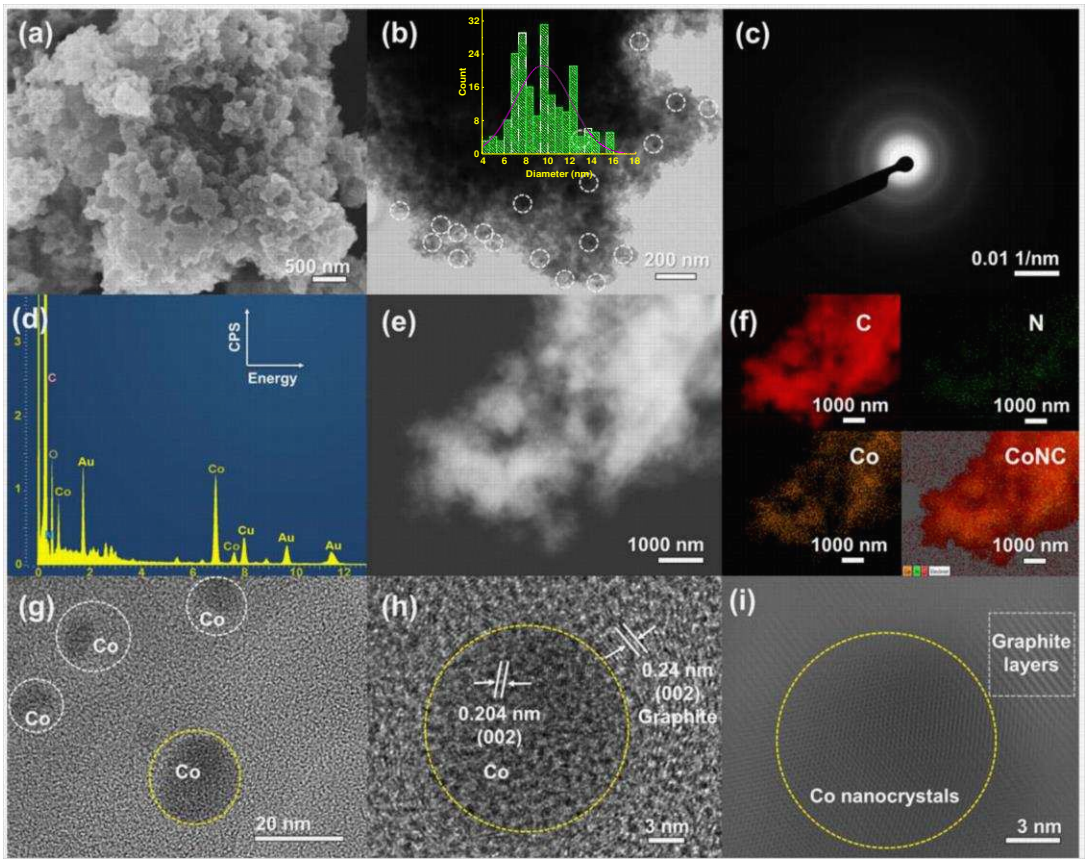

Fig. 2 Characterization of CoNOCs. (a) SEM, (b) TEM, (c) SEAD, (d) EDX, (e) STEM images as well as (f) C, N, Co, and their composite (CoNC) mapping, (g,h) HRTEM and (i) inversed fast Fourier transform (IFFT) contrast enhanced atomic resolution HRTEM images of CoNOC-900. Circled particles (b, g-i) show CoNPs (yellow circle shows the same particle in g,h,i), the square (i) graphitic layers. . The inset on Fig. 2b shows the size distribution of the CoNPs

X-ray photoelectron spectroscopy (XPS) survey spectra confirm the presence of N, O, and C in the CoNOCs (Fig. S7). However, the Co content measured by the surface sensitive XPS is much lower than obtained by ICP/MS measurements (Table S1), indicating again the encapsulation of the CoNPs by carbon layers. In contrast, the Co2p core-level XPS spectrum of CoNOC-900 prepared without acid etching show much more intense peaks associated to metallic Co and CoO (Fig. S8),[25,26] Among the samples, CoNOC-700 exhibits the highest N content with up to 3.65 wt%, as determined by XPS. The N1s core-level XPS spectra of all CoNOCs can be deconvoluted into four individual peaks that are assigned to pyridinic N (~398.4 eV), pyrrolic N (~400.1 eV), graphitic N (~401.2 eV), and oxidized N (~402.9 eV),[27] respectively (Fig. S9a). With increasing pyrolysis temperature the fraction of pyridinic N and pyrrolic N in comparison to the graphitic N decreased. Notably, CoNOC-900 showed a higher fraction of pyridinic and graphitic N compared to NOC-900, i.e. prepared in absence of Co, further supporting that the CoNPs promote graphitization. Such pyridinic and graphitic nitrogen-species are believed to be beneficial for the electrocatalytic activity according to previous studies.[28] The samples

also showed a high amount of oxygen in the carbon lattice (7.2-12.4 wt%), as determined by XPS. Their O1s core-level XPS spectra can be deconvoluted into three peaks at ~531.5, ~532.6, and ~533.6 eV (Fig. S9b), which are assigned to the C-O, N^+-O^-, and C=O bonds of adsorbed water or phenolic hydroxyl groups, oxidized graphitic N, and carbonyl units, respectively.[29,30] According to the N_2 adsorption isotherms (Fig. S10), the Brunauer-Emmett-Teller (BET) surface areas of CoNOC-700, CoNOC-800, CoNOC-900, and CoNOC-1000 are 207, 329, 486, and 394 $m^2\ g^{-1}$ (Table S2), respectively. CoNOC-900 and NOC-900 exhibited similar surface areas (486 *vs.* 458 $m^2\ g^{-1}$). The pore size distribution (PSD) analyses showed that the pore sizes of all materials are mainly smaller than 2 nm (Fig. S11), with micropores contributed >80% to the overall surface area except for CoNOC-1000 due to the highest degree of graphitization. Note that CoNOC-900 and CoNOC-1000 showed an additional outer surface area originating from the interparticular voids, as evidenced by the steep increase of N_2 uptake at relative pressure (p/p_0) above 0.9. Such porosity found on CoNOCs can promote catalytic site exposure and electron transfer, which are favorable for electrocatalysis.[31]

HER performance of CoNOCs. As shown in Fig. 3a, already N,O-dual doped NOC-900 is a good HER catalyst, displaying a low overpotential of 175 mV (Table S3) at 10 mA cm^{-2} i.e. a critical metric in solar fuel production. However, also trace amounts of Pd residues (~0.05 wt%, as determined by ICP) from polymer precursor synthesis can be responsible for the catalytic activity. With the encapsulation of cobalt, CoNOCs exhibit an even better HER activity, as reflected by the large shift of the polarization curves. CoNOC-700, CoNOC-800, CoNOC-900, and CoNOC-1000 show overpotentials (at 10 mA cm^{-2}, η_{10}) of 132, 115, 93, and 102 mV and onset overpotentials (η_{onset}) of 72, 33, 22, and 23 mV (Table S3), respectively, showing that electrocatalysts prepared at 900 ^oC in presence of $Co(acac)_2$ gave the best HER activity (Figs. S12,13). The best η_{10} obtained on CoNOC-900 i.e. 93 mV compares very well to the values obtained on many metal-containing HER carbon electrocatalysts (see detailed comparisons in Table S4),[7,32-37] and is also comparable to the best values recently reported on P-Mo_2C@C nanowires (89 mV)[38] and CoP@BCN-1 nanotubes (87 mV).[39] The Tafel plots of the polarization curves provide insight into the HER pathways on various catalysts (Fig. 3b). The commercial Pt/C electrode exhibit a Tafel slope of 21 mV dec^{-1}, indicating that hydrogen is produced *via* the rate-determining Heyrovsky step ($H^* + H^+ + e^- \rightarrow H_2$ or $H^* + H_2O + e^- \rightarrow H_2 + OH^-$), which is consistent with the known mechanism of HER on Pt.[40] The NOC-900 catalyst showed a Tafel slope of 88 mV dec^{-1}, suggesting that an initial proton adsorption is the rate-determining step ($H^+ + e^- \rightarrow H^*$ or $H_2O + e^- \rightarrow H^* + OH^-$) on the metal-free catalyst.[40] The Tafel analyses of the CoNOC catalysts finally reveal Tafel slopes of 49-75 mV dec^{-1}, indicating that hydrogen is produced *via* the Volmer-Heyrovsky mechanism i.e. the electrochemical desorption is the rate-determining step.[41] On the basis of the Tafel plots, the exchange current density of the catalysts was estimated to be 4.3×10^{-4} A cm^{-2} (Table S3), which is close to that of Pt/C (5.4×10^{-4} A cm^{-2}).[38] The differences in HER electrocatalytic activities of our CoNOC catalysts could be mainly attributed to the electrochemically active surface area (ECSA) and electron transfer rate. Double-layer capacitance (C_{dl}) extracted from the capacitive current as a

function of scan rate is generally used for the estimation of the effective ECSA of the solid/liquid interface, which can be calculated from cyclic voltammetry (CV) curves scanned at different rates.

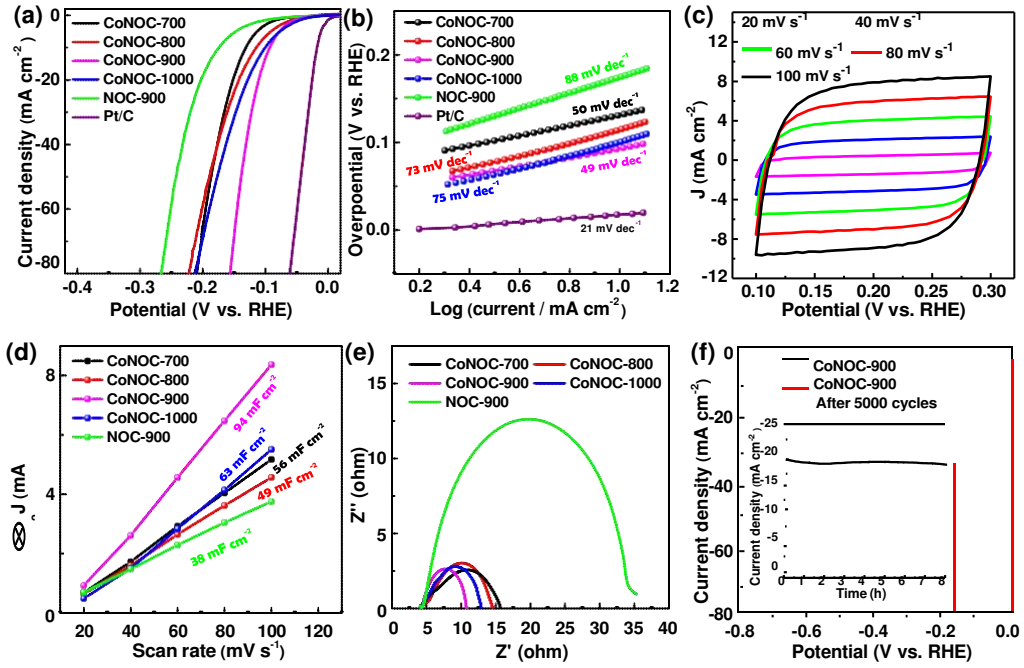

Fig. 3 HER performance of CoNOCs. (a) Polarization curves and (b) corresponding Tafel plots of CoNOC catalysts obtained in 0.5 M H_2SO_4 solution, along with NOC-900 and commercial Pt/C catalysts for comparison; (c) cyclic voltammograms (CV) of CoNOC-900 obtained with different rates from 20-100 mV s^{-1} in a potential range of 0.1-0.3 V without faradaic processes; (d) capacitive current density as functions of scan rate and (e) electrochemical impedance Nyquist plots of for CoNOC catalysts, along with NOC-900 catalyst for comparison; (f) stability tests of CoNOC-900 catalyst upon 5000 potential cycles, inset showing the time dependence of catalytic currents during electrolysis.

As shown in Fig. 3c and Fig. S14, the CV curves of all the catalysts showed roughly rectangular shapes owing to the double-layer capacitance. CoNOC-900 showed the largest C_{dl} of 94 mF cm^{-2} (Fig. 3d), compared to CoNOC-700 (56 mF cm^{-2}), CoNOC-800 (49 mF cm^{-2}), and CoNOC-1000 (63 mF cm^{-2}). The C_{dl} obtained on CoNOC-900 is nearly 2.5 times higher than that of NOC-900 (94 *vs.* 38 mF cm^{-2}), signifying the largest ECSA. Electrical impedance measurements showed the smallest semicircle in the Nyquist plots (Fig. 3e), indicating the lowest charge-transfer resistance. To test the durability of the catalysts in an acidic environment, long-term potential cycling was performed in a 0.5 M H_2SO_4 solution by continuous CV scanning at a rate of 50 mV s^{-1} for 5000 cycles. As shown in Fig. 3f and Fig. S15, although the polarization curves of the CoNOC-700, CoNOC-800, and CoNOC-1000 catalysts showed a slight decay, CoNOC-900 shows a very stable performance, with a negligible loss of current density of 20 mA cm^{-2} over 8 hours (Fig. 3f, inset). Further post mortem characterization including SEM and ICP/MS analyses of catalyst upon 5000 cycling indicated negligible changes in compositions and morphologies (Fig. S16).

Density functional theory (DFT) calculations. The adsorption free energy of H* (ΔG_{H*}) is one of the most important benchmarks determining the HER activity for electrocatalysts.[42,43] A smaller ΔG_{H*} value usually yield a better HER activity and an optimal HER catalyst should have a ΔG_{H*} value close to zero to compromise the reaction barriers of the adsorption and desorption steps. To explain the superior activity of our catalyst and the influence of the present heteroatoms and metal particles, ΔG_{H*} values were calculated for various models including pure graphene (G), N-doped graphene (NG), O-doped graphene (OG), N-doped graphene encapsulated Co (CoNG), and O-doped graphene encapsulated Co (CoOG). Besides, also four possible H* adsorption sites in N,O-dual doped graphene encapsulated Co were calculated (CoNOG-1, 2, 3, and 4). The optimized models are illustrated in Fig. 4a and Figs. S17,18 and the specific ΔG_{H*} values are shown in Table S4. According to the calculated ΔG_{H*} diagram shown in Fig. 4b, the value of ΔG_{H*} decreased strongly already after introduction of N and O dopants in the carbon layers. The combination of a Co metal core and a graphene shell can further decrease the value of ΔG_{H*}. However, N,O-dual doped graphene encapsulated Co exhibits the lowest ΔG_{H*} value among the various models, especially for CoNOG-2 with a value very close to zero. The results show that the introduction of Co, N, and O can remarkably reduce the ΔG_{H*}, explaining the superior HER activity.

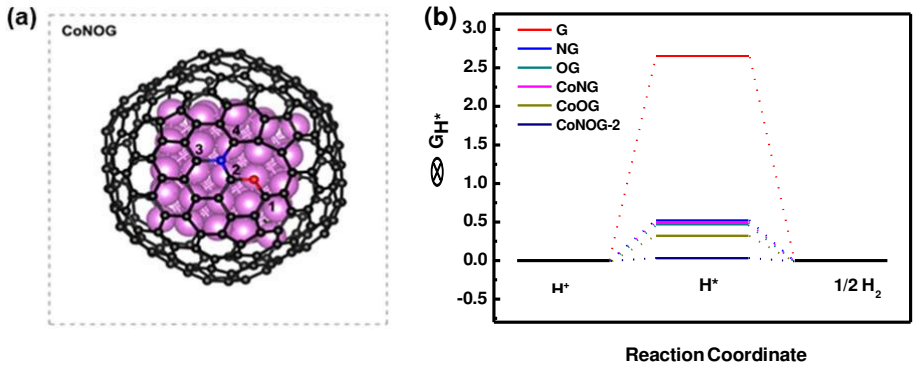

Fig. 4 DFT calculations. (a) Optimized structure of N,O-dual doped graphene encapsulated CoNPs and four possible H* adsorption sites; (b) calculated ΔG_{H*} diagram of various models.

HER performance of CoNOC//CFCs. The use of a polymeric precursor give rise for the fabrication of self-standing membrane-type electrodes by growing the polymer networks on carbon fiber cloth (CFC). As illustrated in Fig. 5a, adding the CFC within the solution of the BH reaction afforded a uniform deposition of PAQTA on the surface of carbon fibers as seen by SEM (Fig. 5b-d). Co impregnation, pyrolysis and acid etching was carried out like the optimized procedure for the bulk materials described before to yield CFC-supported electrodes i.e. CoNOC//CFC-x. As shown in Fig. 5e and the supporting videos, CoNOC//CFC-900 produced hydrogen even faster than CoNOC-900. Indeed, based on the polarization curve measurements, CoNOC//CFC-900 is much more active than CoNOC-900, displaying η_{10} and η_{onset} of 69 and 15 mV, respectively (Fig. 5f). Electrical impedance measurements also indicated a much lower charge-transfer resistance (Fig. 5g). The Tafel slope and exchange current density of CoNOC//CFC-900 were calculated to be 46 mV dec^{-1} and 1.1×10^{-4} A cm^{-}

^{2}, respectively. The promoted electrocatalytic activity can be explained by a very low threshold of conductivity resulting from the binder-free assembly of the membrane-type electrode.

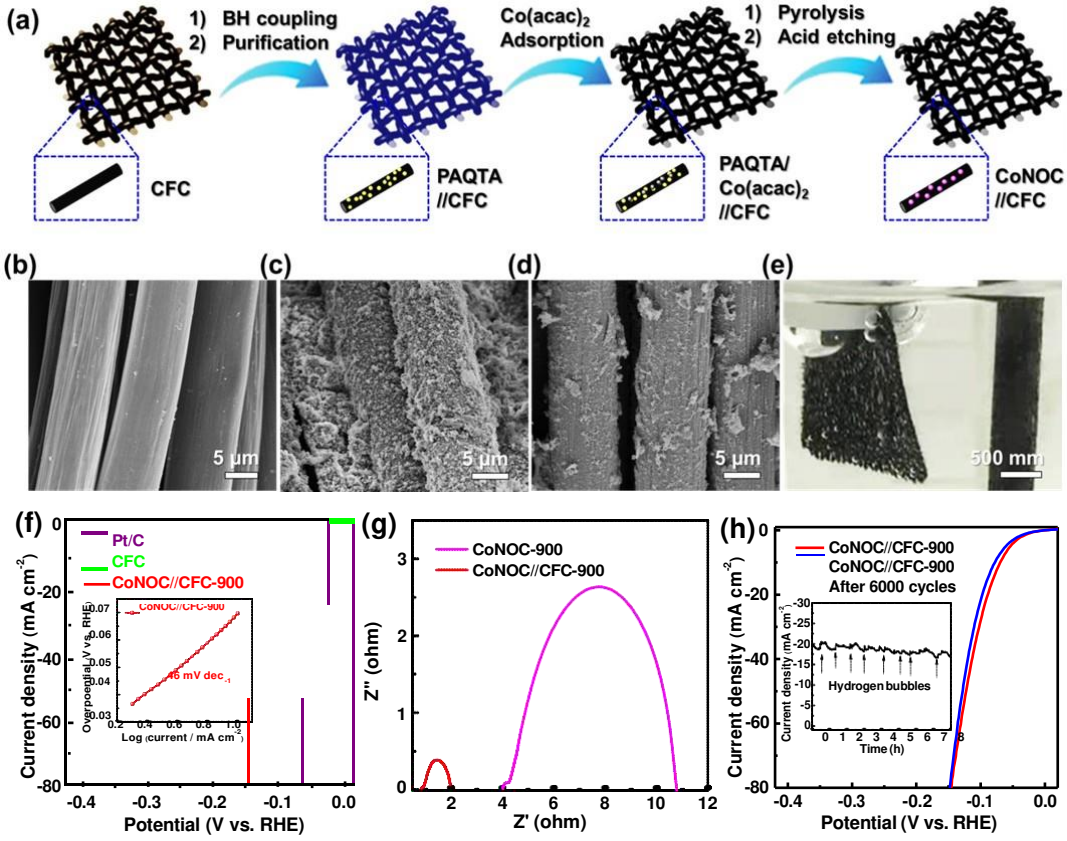

Fig. 5 HER performance of CoNOC//CFCs. (a) Schematic illustration of the synthesis of self-supporting membrane-type CoNOC//CFC electrode, (b) pristine CFC, (c) CFC after PAQTA deposition, (d) PAQTA-deposited CFC upon pyrolysis and acid etching, (e) visible hydrogen production upon applying a 20 mV voltage on CoNOC//CFC-900 for 30 seconds, (f) polarization curves and Tafel plots, (g) Nyquist plots (tested at 5 mV AC potential from 10 kHz to 0.1 Hz), and (h) cyclability of CoNOC//CFC-900.

Although interfered by the large amount of bubbles during the HER, CoNOC//CFC-900 still showed a quite stable current density ca. 19.5 ± 0.5 mA cm^{-2} (only ~2.5% variations) over 8 hours (Fig. 5h), inset), showing an excellent catalytic durability. Overall, the obtained HER activities e.g. η_{10} (69 mV) and Tafel slope (46 mV dec^{-1}) outperforms most recent carbon-based HER catalysts (see detailed comparisons in Table S4).[44-50] As an important feature, the here shown membrane-type electrode could be readily scaled-up owing to the simple *in-situ* deposition, facile pyrolysis, and tailorable CFCs involved. Using such a scaled-up electrode of CoNOC//CFC-900 (1.3 cm × 1.5 cm in size, 50 μm in thickness, and 1.365 mg of active substance), a proof-of-concept demonstration for efficient water splitting is displayed in a supporting video. The electrode roughly produced 4 mL of hydrogen per

minute in a rate of 2.93 L g^{-1} min^{-1} upon applying a 20 mV voltage, making this material promising for environment-friendly hydrogen-production.

In summary, we have developed a simple, low-cost, and efficient route to N,O-dual doped carbons encapsulated cobalt nanoparticles by pyrolysis of an anthraquinonylamine and triphenylamine-based conjugated microporous polymer in presence of cobalt(II) acetylacetonate. The resulting porous carbons with a trace amount of CoNPs exhibited remarkable activity and durability for the hydrogen evolution reaction (HER), which outperforms most of the non-noble metal-based catalysts in acidic solutions. The density functional theory calculations indicated that N,O-dual doping and Co encapsulation significantly decreased the hydrogen adsorption free energy on the surface of the catalysts explaining the superior HER activity. Furthermore, growth of the polymeric pre-catalyst on carbon fiber cloth and subsequent pyrolysis afforded binder-free HER electrode, which was even more active for HER. Owing to the scalability and versatility of the here shown approach, it could be further applied for the rational design of high-performance electrocatalysts for water splitting, batteries, and other electrochemical devices.

Methods

Synthesis of CoNOCs. The precursor PAQTA was synthesized using Buchwald-Hartwig (BH) coupling method.[18] To synthesize the CoNOC catalysts, $Co(acac)_2$ was impregnated in PAQTA pyrolyzed and washed with H_2SO_4. Specifically, 100 mg PAQTA and 771 mg $Co(acac)_2$ were suspended in 30 mL toluene. After stirring the dispersion for 6 h at 80 <, the metal-impregnated CoNOCs were collected by filtration. The resulting powders were pyrolyzed at a temperature of 700, 800, 900 and 1000 <, respectively, for 3 h in a N_2 atmosphere, then etched in 0.5 M H_2SO_4 for 24 h (3 × 8 h), washed with a plenty of water (3 × 200 mL) and then dried at 60 <.

Preparation of CoNOC and CoNOC//CFC electrodes. To prepare the CONOC electrodes using a binder, 5 mg of catalyst was dispersed in a 50 µL 5 wt% Nafion solution (Sigma Aldrich) and 200µL ethanol, and then sonicated to obtain a homogeneous ink. A certain amount of catalyst ink was drop-casted on a polished glassy carbon rotating disk electrode (RDE, Pine, USA, diameter: 5 mm; geometric area: 0.196 cm^2; catalyst loading: ~0.3 mg cm^{-2}) and dried in 50 ^oC oven, affording the CoNOC electrodes. The BH reaction yielded PAQTA-deposited in carbon fibers, providing a host for $Co(acac)_2$ adsorption. Further pyrolysis and acid etching afforded CoNOC//CFC electrodes. Specifically, a Schlenk tube was charged with carbon fiber cloth (CFC, thickness: 0.36 mm, resistance: <1.2 mΩ/cm^2, size: 1.0 cm × 1.5 cm), DAQ (180 mg, 0.75 mmol), TA (245 mg, 0.5 mmol), XPhos (21.5 mg, 0.045mmol), a small amount of $Pd(dba)_2$ (17 mg, 0.03 mmol), and NaOtBu (192 mg, 2 mmol) and placed in N_2 atmosphere. Toluene (50 mL) was added and the reaction was heated to 110 ^oC under stirring for 24 h, then the CFC was removed and washed with DMF, hot MQ water, and $CHCl_3$ (24 h each, 3 × 200 mL) and then dried in a vacuum oven (50 ^oC) for 72 h. The CFC deposited with PAQTA and 771 mg $Co(acac)_2$ were suspended in 30 mL toluene. After stirring the dispersion for 6 h at 80 <, the metal-impregnated CFC was collected by filtration and pyrolyzed at 900 < for 3 h in a N_2

atmosphere. The product was etched in 0.5 M H_2SO_4 for 24 h (3 × 8 h), washed with water (3 × 200 mL) and then dried at 60 <, affording membrane-type electrode CoNOC//CFC-900.

DFT calculations. DFT calculations were carried out using the Vienna Ab Initio Simulation Package (VASP), with supplied Projector Augmented Wave (PAW) potentials for core electrons. The generalized gradient approximation (GGA) of Perdew−Becke−Ernzerhof (PBE) is used for the exchange-correlation functional. A graphitic carbon cage C240 encapsulated 55 metal atoms was used as the model of graphene encapsulated alloys, which performed well in previous study.[6,12] The cut-off energies for plane waves is 400 eV, providing a convergence of 10^{-4} eV in total energy and 0.05 eV/Å in Hellmann Feynman force on each atom. The hydrogen binding energy ΔE_H was calculated by $\Delta E_H = E_{H\text{-slab}} - E_{slab} - 1/2\, E_{H2}$. The free energies at 298.15 K were obtained using $\Delta G_H = \Delta E_H + \Delta ZPE - T\Delta S$, $\Delta E_H = E_{H\text{-slab}} - E_{slab} - 1/2\, E_{H2}$. The free energies at 298.15 K were obtained using $\Delta G_H = \Delta E_H + \Delta ZPE - T\Delta S$=0.3 eV for model of graphene encapsulated metal. according to previous work where ΔE_H is the hydrogen binding energy, ΔZPE, $T\Delta S$ and U are the zero point energy changes and entropy changes, respectively.

Sample characterization. FT-IR spectra were taken on a Nicolet 670 spectrometer. Raman spectra were recorded on a Renishaw InVia Reflex spectrometer. PXRD patterns were obtained on a Bruker D8 Advance diffractometer (40 kV, 30 Ma) using Cu Kα radiation (2θ = 2–90°). XPS were obtained on a Thermo Fisher Scientific ESCALAB 250Xi spectrometer. TGA was carried out on a Mettler Toledo TGA 1 instrument in air in the temperature range 30-1000 °C (heating rate 10 °C/min). SEM images were obtained on a HITACHI S-4800 microscopy. The size distributions and microstructure were analyzed by TEM, HRTEM and SAED on a JEOL-3000F at 300kV. The histogram of the size deviation was generated from a statistical measurement on 200 particles. SAED analysis was performed on JEOL-3000F at 300kV and the camera length was 255.8 mm. HAADF-STEM and XEDS elemental mapping were performed on a JEOL JEM-2100. All specimens were prepared by dispersing samples into ethanol and then drop-casted onto holy carbon supported Au grids. The metal compositions were analyzed using a Leeman Labs Prodigy ICP/MS along with XPS, XEDS, and PXRD. N_2 adsorption/desorption measurements at 77.4 were performed after degassing the samples under high vacuum at 120 °C for 15 hours using a Micro ASAP2046 machine.

Electrochemical measurements. All the electrochemical measurements were performed in a three-electrode system on an electrochemical workstation (Gamry Interface 1100E, USA) in 0.5 M H_2SO_4 at room temperature. All tests were performed with iR compensation. For non-supported catalyst tests, the synthesized catalyst dispersed onto a glass carbon RDE were used as a working electrode, a saturated calomel electrode (SCE) was used as the reference electrode, and a graphite rod was served as the counter electrode. Linear sweep voltammetry (LSV) scans with a rate of 5 mV s^{-1} was conducted after purged the electrolyte solutions for 30 min ensuring the complete elimination of dissolved oxygen. During the measurements, the headspace of the electrochemical cell was continuously purged with N_2. Electrochemical impedance spectroscopy (EIS) Nyquist plots were obtained by carrying out the measurements in the same configuration at η = 0.15 V from 10^5-0.1 Hz with an AC voltage of 5 mV.

The stability testing of the catalysts were examined by continuously cycling the potential between +0.1 and −0.5 V *vs.* RHE at a scan rate of 50 mV/s while the time-dependent stability were operated at a constant current density of 20 mA cm^{-2}. For self-supporting catalyst test, the membrane-type catalyst was directly used as the working electrode. The LSV, EIS, and stability measurements were carried out as same as that procedure applied for non-supported catalyst tests. All of the potentials were calculated according to $E_{RHE} = 0.242 + 0.059$ pH. The Tafel slope was calculated from polarization curves on the basis of the Tafel equation: $\eta = a + b \log j$, where η is the overpotential (mV), b is the Tafel slope, j is the current density (mA cm^{-2}). Moreover, the exchange current density (j_0) was obtained by extrapolation of Tafel plots ($\eta = 0$, $j_0 = 10^{(-a/b)}$). Double-layer capacitance (C_{dl}) was obtained by cyclic voltammetry measurements in the potential range of 0.1 to 0.3 V *vs.* RHE with scan rates from 20 to 100 mV s^{-1}. The capacitive currents of $\Delta J_{|Ja-Jc|}/2$ at 0.2 V *vs.* RHE were plotted against the scan rates. The slope of the curves was the double-layer capacitance.

Data availability. The data that support this paper and other findings of this study are available from the corresponding author upon reasonable request.

References

1. Lu, Q. P. et al. 2D Transition-metal-dichalcogenide-nanosheet-based composites for photocatalytic and electrocatalytic hydrogen evolution reactions. *Adv. Mater.* **28**, 1917-1933 (2016).
2. Hinnemann, B. et al. Biomimetic hydrogen evolution: MoS_2 nanoparticles as catalyst for hydrogen evolution. *J. Am. Chem. Soc.* **127**, 5308-5309 (2005).
3. Chen, W. F. et al. Hydrogen-evolution catalysts based on non-noble metal nickel-molybdenum nitride nanosheets. *Angew. Chem. Int. Ed.* **51**, 6131-6135 (2012).
4. Cao, B. F. et al. Mixed close-packed cobalt molybdenum nitrides as non-noble metal electrocatalysts for the hydrogen evolution reaction. *J. Am. Chem. Soc.* **135**, 19186-19192 (2013).
5. Le, G. A. et al. From hydrogenases to noble metal-free catalytic nanomaterials for H_2 production and uptake. *Science* **326**, 1384-1387 (2009).
6. Deng, J., Ren, P. J., Deng, D. H. & Bao, X. H. Enhanced electron penetration through an ultrathin graphene layer for highly efficient catalysis of the hydrogen evolution reaction. *Angew. Chem. Int. Edit.* **54**, 2100-2104 (2015).
7. Deng, J. et al. Highly active and durable non-precious-metal catalysts encapsulated in carbon nanotubes for hydrogen evolution reaction. *Energy Environ. Sci.* **7**, 1919-1923 (2014).
8. Tavakkoli, M. et al. Single< shell carbon< encapsulated iron nanoparticles: synthesis and high electrocatalytic activity for hydrogen evolution reaction. *Angew. Chem. Int. Edit.* **54**, 4535-4538 (2015).
9. Wang, J. et al. Non-noble metal-based carbon composites in hydrogen evolution reaction: fundamentals to applications. *Adv. Mater.* **29**, 1605838 (2017).
10. Chung, D. Y. et al. Large-scale synthesis of carbon-shell-coated FeP nanoparticles for robust hydrogen evolution reaction electrocatalyst. *J. Am. Chem. Soc.* **139**, 6669-6674 (2017).

11. Wang, J. H. et al. Recent progress in cobalt-based heterogeneous catalysts for electrochemical water splitting. *Adv. Mater.* **28**, 215-230 (2016).
12. Su, J. W. et al. Ruthenium-cobalt nanoalloys encapsulated in nitrogen-doped graphene as active electrocatalysts for producing hydrogen in alkaline media. *Nat. Commun.* **8**, 14969 (2017).
13. Zhang, L. L., Xiao, J., Wang, H. Y. & Shao, M. H. Carbon-based electrocatalysts for hydrogen and oxygen evolution reactions. *ACS Catal.* **7**, 7855-7865 (2017).
14. Lu, C. B. et al. Molybdenum carbide-embedded nitrogen-doped porous carbon nanosheets as electrocatalysts for water splitting in alkaline media. *ACS Nano* **11**, 3933-3942 (2017).
15. Qu, K. G. et al. Polydopamine-inspired, dual heteroatom-doped carbon nanotubes for highly efficient overall water splitting. *Adv. Energy Mater.* **7**, 1602068 (2017).
16. Chaoui, N. et al. Trends and challenges for microporous polymers. *Chem. Soc. Rev.* **46**, 3302-3321 (2017).
17. Xu, F., Wu, D. C., Fu, R. W. & Wei, B. Q. Design and preparation of porous carbons from conjugated polymer precursors. *Nano Today* **20**, 629-656 (2017).
18. Liao, Y. Z., Wang, H. G., Zhu, M. F. & Thomas, A. Efficient supercapacitor energy storage using conjugated microporous polymer networks synthesized from Buchwald-Hartwig coupling. *Adv. Mater.* **1705710** (2018).
19. Zou, X. X. et al. Cobalt-embedded nitrogen-rich carbon nanotubes efficiently catalyze hydrogen evolution reaction at all pH values. *Angew. Chem.* **126**, 4461-4465 (2014).
20. Yang, H. B. et al. Identification of catalytic sites for oxygen reduction and oxygen evolution in N-doped graphene materials: development of highly efficient metal-free bifunctional electrocatalysts. *Sci. Adv.* **2,** e1501122 (2016).
21. Yang, Y. et al. Tuning electronic structures of nonprecious ternary alloys encapsulated in graphene layers for optimizing overall water splitting activity. *ACS Catal.* **7**, 469-479 (2017).
22. Ma, J.-L., Meng, F.-L., Xu, D. & Zhang, X.-B. Co-embedded N-doped carbon fibers as highly efficient and binder free cathode for Na-O_2 batteries. *Energy Storage Mater.* **6**, 1-8 (2017).
23. Hou, B. et al. Structure and band edge energy of highly luminescent CdSe1–xTex alloyed quantum dots. *J. Phys. Chem. C* **117**, 6814-6820 (2013).
24. Zeng, M. et al. Metallic cobalt nanoparticles encapsulated in nitrogen-enriched graphene shells: its bifunctional electrocatalysis and application in zinc-air batteries. *Adv. Funct. Mater.* **26**, 4397-4404 (2016).
25. Wang, J. et al. CoO_x–carbon nanotubes hybrids integrated on carbon cloth as a new generation of 3D porous hydrogen evolution promoters. *J. Mater. Chem. A* **5**, 10510-10516 (2017).
26. Zhang, P. et al. 3D hierarchical Co/CoO-graphene-carbonized melamine foam as a superior cathode toward long-life lithium oxygen batteries. *Adv. Funct. Mater.* **26**, 1354-1364 (2016).
27. Zhang, J. T. & Dai, L. M. Nitrogen, phosphorus, and fluorine tri< doped graphene as a multifunctional catalyst for self< powered electrochemical water splitting. *Angew. Chem. Int. Ed.* **55**, 13296-13300 (2016).

28. Li, S. et al. 2D porous carbons prepared from layered organic-inorganic hybrids and their use as oxygen-reduction electrocatalysts. *Adv. Mater.* **29**, 1700707 (2017).
29. Hulicova-Jurcakova, D., Seredych, M., Lu, G. Q. & Bandosz, T. J. Combined effect of nitrogen- and oxygen-containing functional groups of microporous activated carbon on its electrochemical performance in supercapacitors. *Adv. Funct. Mater.* **19**, 438-447 (2009).
30. Guedidi, H. et al. The effects of the surface oxidation of activated carbon, the solution pH and the temperature on adsorption of ibuprofen. *Carbon* **54**, 432-443 (2013).
31. Liang, H.-W. et al. Mesoporous metal-nitrogen-doped carbon electrocatalysts for highly efficient oxygen reduction reaction. *J. Am. Chem. Soc.* **135**, 16002-16005 (2013).
32. Liu, Y. P. et al. Coupling Mo_2C with nitrogen-rich nanocarbon leads to efficient hydrogen-evolution electrocatalytic sites. *Angew. Chem. Int. Ed.* **54**, 10752-10757 (2015).
33. Yang, J. et al. Porous molybdenum phosphide nano-octahedrons derived from confined phosphorization in UIO-66 for efficient hydrogen evolution. *Angew. Chem.* **128,** 13046-13050 (2016).
34. Wang, Z.-L. et al. C and N hybrid coordination derived Co-C-N complex as a highly efficient electrocatalyst for hydrogen evolution reaction. *J. Am. Chem. Soc.* **137**, 15070-15073 (2015).
35. Liang, H. W. et al. Molecular metal–N_x centres in porous carbon for electrocatalytic hydrogen evolution. *Nat. Commun.* **6**, 7992 (2015).
36. Han, Q. et al. Mesh-on-mesh graphitic-C_3N_4@graphene for highly efficient hydrogen evolution. *Adv. Funct. Mater.* **27**, 1606352 (2017).
37. Qu, K. G. et al. Promotion of electrocatalytic hydrogen evolution reaction on nitrogen-doped carbon nanosheets with secondary heteroatoms. *ACS Nano* **11**, 7293-7300 (2017).
38. Shi, Z. P. et al. Phosphorus-Mo_2C@carbon nanowires toward efficient electrochemical hydrogen evolution: composition, structural and electronic regulation. *Energy Environ. Sci.* **2017**, **10**, 1262-1271.
39. Tabassum, H. et al. Metal-organic frameworks derived cobalt phosphide architecture encapsulated into B/N Co-doped graphene nanotubes for all pH value electrochemical hydrogen evolution. *Adv. Energy Mater.* **7**, 1601671 (2017).
40. Conway, B. E. & Tilak, B. V. Interfacial processes involving electrocatalytic evolution and oxidation of H_2, and the role of chemisorbed H. *Electrochim. Acta* **47**, 3571-3594 (2002).
41. Deng, D. H. et al. Catalysis with two-dimensional materials and their heterostructures. *Nat. Nanotech.* **11**, 218-230 (2016).
42. Jiao, Y., Zheng, Y., Davey, K. & Qiao, S.-Z. Activity origin and catalyst design principles for electrocatalytic hydrogen evolution on heteroatom-doped graphene. *Nat. Energy* **1**, 16130 (2016).
43. Yang, Y. et al. Non-precious alloy encapsulated in nitrogen-doped graphene layers derived from MOFs as an active and durable hydrogen evolution reaction catalyst. *Energy Environ. Sci.* **8**, 3563-3571 (2015).

44. Wang, X.-D. et al. Novel porous molybdenum tungsten phosphide hybrid nanosheets on carbon cloth for efficient hydrogen evolution. *Energy Environ. Sci.* **9**, 1468-1475 (2016).
45. Xiang, Z. C. et al. MoS_2 nanosheets array on carbon cloth as a 3D electrode for highly efficient electrochemical hydrogen evolution. *Carbon* **98**, 84-89 (2016).
46. Huang, X. L. et al. Activating basal planes and S-terminated edges of MoS_2 toward more efficient hydrogen evolution. *Adv. Funct. Mater.* **27**, 1604943 (2017).
47. Yan, X.-Y. et al. Self-supported rectangular CoP nanosheet arrays grown on a carbon cloth as an efficient electrocatalyst for the hydrogen evolution reaction over a variety of pH values. *New J. Chem.* **41**, 2436-2442 (2017).
48. Zhang, Y. Q. et al. Ultrafine metal nanoparticles/N-doped porous carbon hybrids coated on carbon fibers as flexible and binder-free water splitting catalysts. *Adv. Energy Mater.* **7**, 1700220 (2017).
49. Yan, J. J. et al. $MoSe_2$ nanosheets grown on polydopamine-derived porous fibers: a high-performance catalyst for hydrogen evolution reaction. *Adv. Mater. Interfaces* **4**, 1600825 (2017).
50. Ren, B. W. et al. Novel porous tungsten carbide hybrid nanowires on carbon cloth for high-performance hydrogen evolution. *J. Mater. Chem. A* **5**, 13196-13203 (2017).

Acknowledgments

This work was supported by the National Natural Science Foundation of China (51673039), the Shanghai Pujiang Talent Program (16PJ1400300), the Shanghai Key Fundamental Project (16JC1400700/01) and the Fundamental Research Funds for the Central Universities (16D110618). We furthermore acknowledge the support from the Sino-German Center for Research Promotion (GZ879).

Author contributions

Y.L. proposed the idea behind the research and supervised the project. H.W. and B.H. performed the synthesis, characterization and measurements. Y.Y. carried out the model construction and DFT calculations. All authors co-wrote the paper, discussed the results and commented on the manuscript.

Competing interests

The authors declare no competing financial interests.

Additional information

Supplementary information. Tables for elemental composition, porosity, catalytic activity summaries and comparisons, SEM, TEM, HRTEM and STEM images, element mapping, XPS spectra, nitrogen adsorption/desorption isotherms, pore size distribution, CV curves, electrocatalytic durability tests, and DFT calculations. This material is available free of charge *via* the Internet at www.nature.com.